Journal of Materials Chemistry A



PAPER

View Article Online
View Journal | View Issue



Cite this: J. Mater. Chem. A, 2022, 10, 4992

Effective aperture tuning of a zeolitic-imidazole framework CdIF-1 by controlled thermal amorphization†

Sunghwan Parka and Hae-Kwon Jeong ** **

Sodalite zeolitic-imidazole frameworks (ZIFs) show great potential due to their effective aperture sizes suitable for small gas separations. Numerous efforts have, therefore, been made in tuning their effective aperture sizes to control and enhance their molecular sieving properties. Herein, we present a new strategy to finely tune the effective aperture size of CdIF-1, a cadmium-substituted ZIF-8 analogue, based on thermal amorphization. Among several ZIF-8 analogues screened, CdIF-1 was found to be the only one that could be thermally amorphized. The controlled amorphization reduced the long-range structural order while preserving the short-range order, thereby systematically densifying the ZIF structure and consequently affecting its effective aperture. Meanwhile, it was found that amorphization enhanced the flexibility of the framework, resulting in accessible pores at temperatures above 273 K. As compared to its crystalline counterpart, partially amorphized CdIF-1 showed significantly improved diffusion and adsorption selectivities of n-C₄H₁₀/i-C₄H₁₀ (i.e., 1.5 \rightarrow 40.7 and 1.1 \rightarrow 4.9, respectively), likely due to the amorphization-induced tuning of its effective aperture size.

Received 16th December 2021 Accepted 26th January 2022

DOI: 10.1039/d1ta10706b

rsc.li/materials-a

Introduction

Zeolitic-imidazole frameworks (ZIFs) are a sub-class of crystalline nanoporous metal-organic frameworks (MOFs) with zeolite-like topologies.¹⁻³ ZIFs consist of divalent transition metal ions tetrahedrally coordinated with imidazolate-derived ligands. In particular, ZIFs with a sodalite (SOD) topology have drawn considerable research interest for their gas separation applications primarily due to their effective apertures in the scale of important gas molecules.4 For example, ZIF-8, made of zinc ions and 2-methylimidazolate (mIm), showed an impressive molecular sieving effect for propylene/propane separation due to its effective aperture size of \sim 4.0 Å, that is in between the molecular sizes of propylene and propane. 5,6 As with any other crystalline molecular sieves such as zeolites, however, ZIFs suffer from a fundamental limitation in that their sieve sizes (i.e., aperture sizes) are available in a discrete manner. In other words, a ZIF with a proper sieve size for a specific gas mixture might not be available.

One way to overcome the above-mentioned limitation is to fine-tune the aperture sizes of ZIFs. In fact, several strategies have been developed to fine-tune the aperture size of ZIF-8.4 One

such strategy is the substitution or mixing of organic linkers and/or metal centers in the framework while preserving the SOD topology.⁷ For instance, the systematic mixing of 2-methylimidazolate (mIm) and bulkier benzimidazolate (bIm) led to an orderly reduction in the effective aperture size of the resulting mixed-linker ZIF-7-8.⁸⁻¹⁰ Likewise, mixing Zn²⁺ and Co²⁺ enabled the tuning of the effective apertures of the mixed-metal ZIF-8-67.^{11,12} Another effective strategy is to restrict the flexibility of the ZIF-8 framework by an electric field^{13,14} or a rapid heat treatment,¹⁵ thereby enhancing its molecular sieving effect. Yet another strategy is to impregnate the cages of ZIF-8 with ionic liquid, resulting in a reduced effective aperture.¹⁶

Amorphous ZIFs (aZIFs) including ZIF-glasses (a_gZIFs) are an emerging class of new materials with great potential because of their enhanced mechanical/chemical stabilities and their processibility in the molten state. ¹⁷⁻¹⁹ Despite the absence of the long-range order, aZIFs are chemically identical to their crystalline counterparts and maintain the short-range order. ^{20,21} Some crystalline ZIFs can be irreversibly transformed into aZIFs by diverse means such as heating, ball-milling, pressure, and irradiation of an electron beam or X-ray. ^{18,22-25} As the crystallinities of the ZIFs disappear, the densities of the frameworks increase. The amorphization-induced framework densification often led to a substantial loss in their porosities, ^{21,23} although there were a few reports on aZIFs maintaining limited accessible porosities. ^{19,26-29}

Not all amorphization processes can lead to the amorphization of specific ZIFs. Given its importance as a prototypical sodalite (SOD) ZIF, amorphization of ZIF-8 is of particular

^aArtie McFerrin Department of Chemical Engineering, Texas A&M University, 3122 TAMU, College Station, TX 77843-3122, USA

^bDepartment of Materials Science and Engineering, Texas A&M University, 3122 TAMU, College Station, TX 77843-3122, US. E-mail: hjeong7@tamu.edu

[†] Electronic supplementary information (ESI) available. See DOI: 10.1039/d1ta10706b

interest. Readily available processes such as heating and ballmilling resulted in decomposition of ZIF-8 and formation of virtually non-porous aZIF-8 (known as a_mZIF-8), respectively.²¹ Amorphization at high pressures (0.9 and 1.2 GPa) led to the formation of aZIF-8 (named apZIF-8) with much reduced accessible porosity.21,30 Nonetheless, there are no studies reported on the adsorption and diffusion of gas molecules on the pressure-induced a_pZIF-8.^{26,27} It is noted that pressure-induced amorphization of ZIF-8 is not as simple, practical, and controllable as thermal amorphization. Furthermore, there have been no reports on tuning the molecular sieving properties of ZIF-8 and its isostructures (i.e., ZIFs with the same SOD structures but composed of different metal centers or linkers) using controlled thermal amorphization.

CdIF-1 is isostructural to ZIF-8 made of Cd²⁺ ions, instead of Zn²⁺, as a metal center. Due to its more flexible and elongated metal-ligand bonds,31 CdIF-1 exhibits a larger aperture size (i.e., 3.9-4.2 Å)¹² than other isostructures with different metal centers such as ZIF-8 and ZIF-67 (Co-substituted ZIF-8). Baxter et al.32 reported amorphous CdIF-1 by ball-milling (i.e., a_mCdIF-1). They found that unlike aZIF-8 where the environment of zinc was similar to that of ZIF-8, the environment of cadmium in a_mCdIF-1 was different from that in its crystalline counterpart.³² The gas adsorption/diffusion properties of a_mCdIF-1 have not been reported.

In this work, we present the first example of thermallyinduced amorphization of CdIF-1 with accessible porosity. Furthermore, we show that controlled thermal amorphization can lead to the tuning of the effective aperture size of the

thermally amorphized CdIF-1 (i.e., a_TCdIF-1). The amorphization process was systematically investigated by varying heat treatment conditions. Physicochemical and gas adsorption/ transport properties of a_TCdIF-1 with varying degrees of amorphization were thoroughly characterized and compared with those of its crystalline counterpart, CdIF-1.

Results and discussion

To investigate the possibility of thermal amorphization of ZIF-8 isostructures (hereafter, iso-ZIF-8s), we investigated a number of iso-ZIF-8s including ZIF-7, ZIF-8, ZIF-67, CdIF-1, and Co/Zn and Cd/Zn mixed-metal ZIFs. It was found that only CdIF-1 (Fig. 1a and b) could be thermally transformed into an amorphous phase presumably due to its relatively weak and flexible framework (Fig. 1c). 33-35 To the best of our knowledge, this is the first report on the relatively simple thermal amorphization of a ZIF-8 isostructure.21,22,36

Fig. 1d shows the DSC and TGA results of CdIF-1 upon a heat-treatment. The DSC curve showed an endothermic peak corresponding to the amorphization temperature (T_a) at \sim 220 °C, strongly indicating the thermal amorphization of CdIF-1. It is noted here that none of the other iso-ZIF-8s with different metal centers, such as ZIF-8, ZIF-67, and mixed-metal ZIFs (Co/ Zn-ZIF-8 and Cd/Zn-ZIF-8), showed amorphization at temperature below the carbonization (or decomposition) temperature (Fig. S1 and S2†). The CdIF-1 sample treated at 220 °C showed negligible change in the XRD intensity when it was cooled immediately (denoted as 0 min in Fig. S1†). As the soaking time

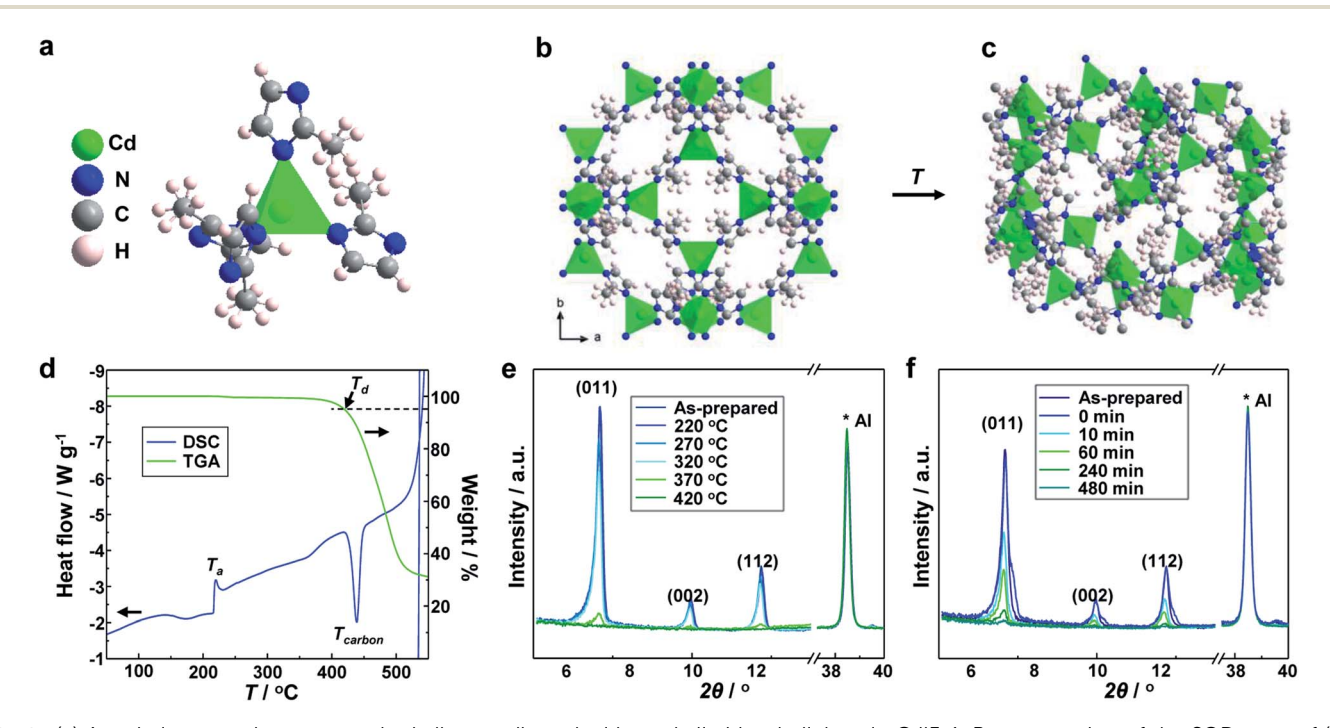


Fig. 1 (a) A cadmium metal center tetrahedrally coordinated with methylimidazole linkers in CdIF-1. Representation of the SOD cage of (b) crystalline CdIF-1 and (c) hypothetical amorphous CdIF-1 (aCdIF-1). (d) Thermograms of the DSC (1st upscan), and TGA for CdIF-1. XRD patterns of the CdIF-1 samples treated at different temperatures with 0 min soaking time (e) and treated at a fixed temperature of 320 °C for different soaking times (f).

increased to 12 h at 220 °C, however, the XRD intensity noticeably decreased (Fig. S3†), suggesting that $\sim\!\!220$ °C is the onset temperature of amorphization under the current conditions. The second scan of the DSC curve exhibited the melting temperature at $\sim\!\!320$ °C (Fig. S4a†). It is noted that this is not the melting point of aCdIF-1, but that of an unknown carbonized cadmium compound since CdIF-1 was heated beyond the degradation temperature ($T_{\rm d}$) of $\sim\!\!420$ °C upon the first scan (Fig. S4†).

When the heat-treatment temperature increased, the XRD intensities decreased continuously, indicating that CdIF-1 was irreversibly transformed into partially amorphous CdIF-1 (a_T-CdIF-1) with a different extent of amorphization (Fig. 1e). It is noted that the extent of amorphization was determined based on the relative (110) intensity of the sample to that of the pristine CdIF-1.37 Nevertheless, there was an abrupt drop in the XRD intensity between 320 °C and 370 °C, making it difficult to precisely control the amorphization process in this temperature range (Fig. 1e and S5a†). In addition, there was considerable degradation when CdIF-1 was treated at 420 °C (Fig. S6a†), which was also confirmed by the color change (Fig. S7†). On the other hand, a more controlled amorphization was achieved by varying the soaking time at a fixed temperature of 320 °C (Fig. 1f and S5b†) with a minor weight loss of ~5 wt% (Fig. S6b and S8†). Hereafter, the a_TCdIF-1 samples treated at 320 °C for 0 min, 60 min, and 480 min are denoted as a_{0.3}CdIF-1, a_{0.7}CdIF-1, and a_{1.0}CdIF-1, respectively, in which the subscript numbers indicate the extents of amorphization.

Fig. S9† presents the XRD patterns of the a_T CdIF-1 samples. As the extent of amorphization increased (*i.e.*, the crystallinity decreased), a new broad peak emerged at 2θ of 13.96° (*d*-spacing \sim 6.34 Å), suggesting the preservation of the short-range order.

The emergence of a new broad peak is consistent with the cases of other aZIFs.²³ The broad peak corresponds to the Cd–Cd distance of crystalline CdIF-1 (*i.e.*, 6.4 Å).³¹ Baxter *et al.*³² reported that when mechanically amorphized, a_mCdIF-1 exhibited quite different FT-IR spectra from the CdIF-1 due to the rearrangement of the short-range order in the vicinity of Cd²⁺. In stark contrast, the FT-IR spectra of the a_TCdIF-1 and the CdIF-1 samples are virtually the same, indicating that they are chemically identical. As the extent of amorphization increased, however, the Cd–N band was red-shifted (see the spectra on the right in Fig. S10†). This implies that the Cd–N bonds became soft upon amorphization, consequently increasing the framework flexibility.

Fig. S11 and S12† present the SEM and TEM images of the CdIF-1 and the a_T CdIF-1 particles. The CdIF-1 particles were intergrown with an average size of \sim 1 μ m. As can be seen in Fig. S11,† the a_T CdIF-1 samples were similar in size and morphology to CdIF-1. To examine any structural changes, HRTEM images were recorded. As shown in Fig. 2, a gradual loss in crystallinity was observed as the extent of amorphization increased. Fig. S13† presents fast-Fourier-transform (FFT) diffractions from different locations of the selected part of the $a_{0.3}$ CdIF-1 sample, showing varying degrees of amorphization depending on the location of the sample. This implies that amorphization proceeds not necessarily from the external surfaces but likely from the more defective sites (either external or internal). 35

Fig. 3a presents N_2 physisorption of the a_T CdIF-1 samples at 77 K, showing drastic reduction in their specific gas uptakes as the extent of amorphization increased, strongly suggesting the structural densification upon amorphization (Table S1†). ^{22,23} In contrast, the C_3H_8 isotherms at 273 K (Fig. 3b and S14†)

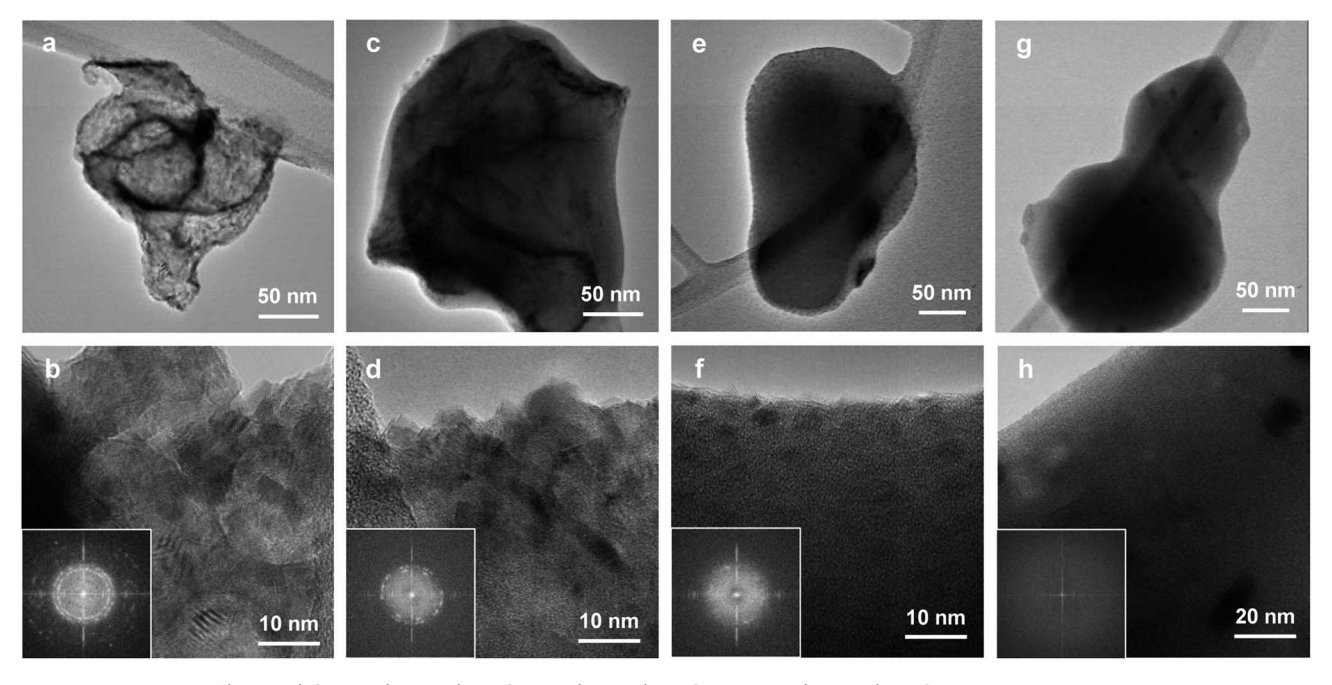


Fig. 2 HRTEM images of (a and b) CdIF-1, (c and d) $a_{0.7}$ CdIF-1, (e and f) $a_{0.7}$ CdIF-1, and (g and h) $a_{1.0}$ CdIF-1. The insets in the lower images are the corresponding FFT diffraction patterns.

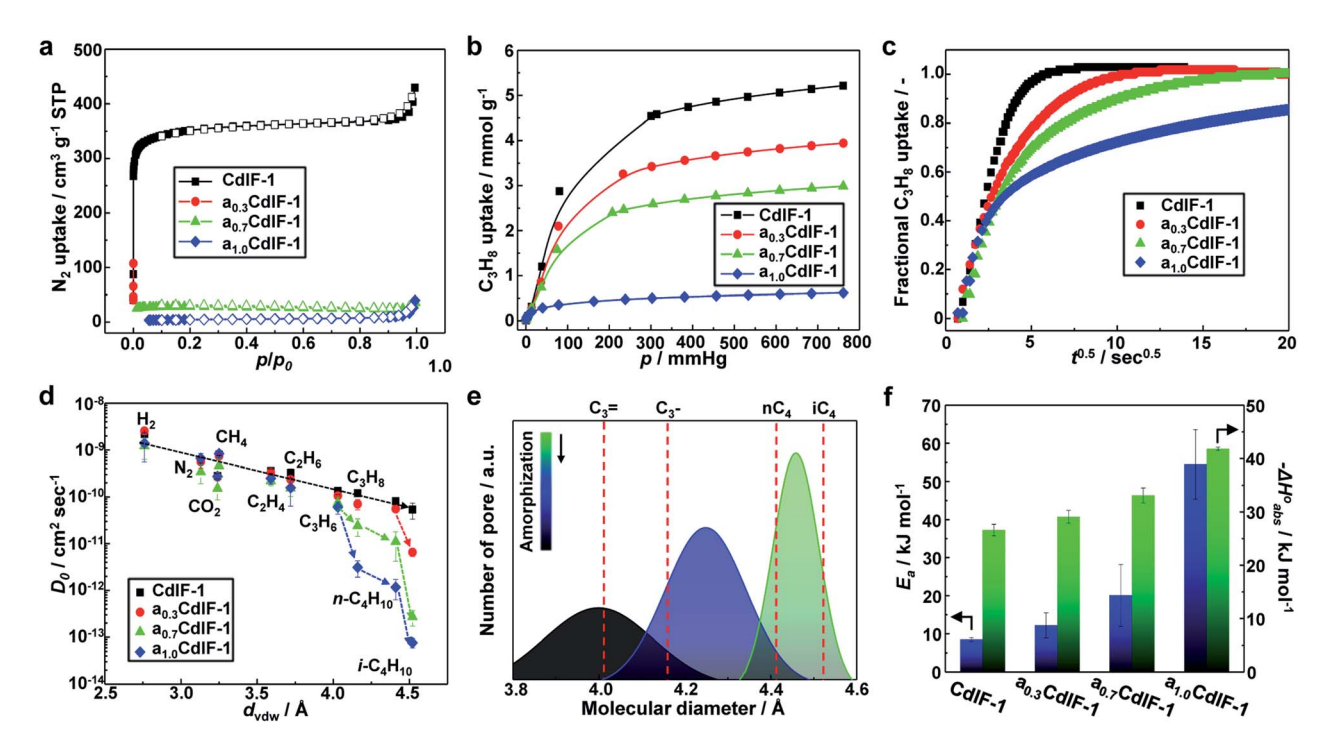


Fig. 3 (a) N_2 adsorption isotherms at 77 K, (b) C_3H_8 adsorption isotherms at 273 K, (c) C_3H_8 kinetic adsorption at 273 K at a fixed dosing pressure of 0.5 mmHq, (d) corrected diffusivities as a function of van der Waals diameters of gas molecules, (e) hypothetical pore size distributions with the different extents of amorphization, and (f) the activation energies of diffusion (E_a) and the isosteric heats of adsorption (ΔH_{ads}^2) of C_3H_8 for the CdIF-1 and the a_TCdIF-1 samples.

indicate that the a_TCdIF-1 samples possess accessible pores at 273 K, which decreased as the extent of amorphization increased. This observation can be attributed to the fact that the enhanced flexibility of the frameworks of a_TCdIF-1 due to its softened Cd-N bonds enables the adsorption of gas molecules despite their densified structures.38 Fig. S14† presents adsorption isotherms of various gas molecules of different sizes, showing the more pronounced effects of amorphization on the adsorption of the larger gas molecules due to the more limited access of the larger molecules.

Fig. 3c and S15† present the kinetic uptakes of different gas molecules for both CdIF-1 and a_TCdIF-1 samples. As can be seen in the figures, the greater the extent of amorphization, the lower the slope of the kinetic uptake curve for the larger gases. In contrast, there were no significant differences for the smaller gases. Based on the kinetic and equilibrium adsorption results (Table S2 \dagger), the corrected diffusivities (D_0) of gas molecules were calculated and are presented in Fig. 3d and Table S3.† As shown in Fig. 3d, the corrected diffusivities of CdIF-1 were monotonically decreased as the size of the tested gas increased. However, the a_TCdIF-1 samples showed a drastic decrease at certain sizes of gas molecules, depending on the extent of amorphization. A sharp reduction in the corrected diffusivity appeared for i-C₄H₁₀ (4.52 Å) in the case of a_{0.3}CdIF-1, for n- C_4H_{10} (4.41 Å) in the case of $a_{0.7}CdIF-1$, and for C_3H_8 (4.16 Å) in case of a_{1.0}CdIF-1 (Fig. 3d). This demonstrates that there exist the so-called molecular cut-offs which were shifted toward the smaller gas molecules as the extent of amorphization increased (Fig. 3e). In other words, as the extent of amorphization

increased, the effective aperture size of a_TCdIF-1 decreased while the size distribution was likely broadened as illustrated in Fig. 3e.

Consequently, the n-C₄H₁₀/i-C₄H₁₀ diffusivity selectivity of a_TCdIF-1 was changed from 1.5 to 8.5, to 40.7, and to 15.3 as the extent of amorphization increased to 30%, to 70%, and to 100%, respectively. In addition, the n-C₄H₁₀/i-C₄H₁₀ adsorption selectivity of a_TCdIF-1 increased more than four-fold as the extent of amorphization increased (Fig. S16†). Interestingly, the enhancement of the C4 adsorption selectivities was much greater at low pressures and reached a constant value (Fig. S16†), indicating the heterogeneity of additional adsorption sites favoring n-C₄H₁₀ formed upon amorphization. These observations strongly suggest that controlled amorphization could tune the effective aperture size of CdIF-1, resulting in controllable molecular sieving effects.

The tunable molecular sieving effects of a_TCdIF-1 were investigated in terms of kinetic and thermodynamic factors (Fig. S17-S21†). As the extent of amorphization increased, the isosteric heat of adsorption increased likely due to the enhanced interaction between the micropores and the gas molecules resulting from densification (Fig. 3f and Table S4†).39,40 On the other hand, the activation energy of diffusion increased more dramatically (Fig. 3f and Table S5†). It is noted that the sizes of gas molecules had a much more critical effect on the activation energy of diffusion than on the isosteric heat of adsorption (Table S4 and S5†), indicating that gas transport a_TCdIF-1 is dominated by kinetics rather than thermodynamics.

Experimental

Materials

Cadmium nitrate tetrahydrate (Cd(NO₃)₂·4H₂O, hereafter CdN, 98%, Sigma Aldrich), 2-methylimidazole (C₄H₆N₂, hereafter HmIm, 99%, Sigma Aldrich), triethylamine ((C₂H₅)₃N, TEA, 99%, Alfa Aesar), and methanol (CH₃OH, MeOH, >99.8%, Alfa Aesar) were used as received.

Synthesis of CdIF-1

CdIF-1 was synthesized by following a method found in our previous report.41 Briefly, metal and ligand solutions were prepared by dissolving 0.761 g of CdN in 20 ml MeOH and by dissolving 1.622 g of HmIm in 20 ml MeOH with 0.5 g of TEA, respectively. After mixing the two solutions, the resulting solution was subjected to a solvothermal reaction at 60 °C for 7 h in a Teflon-lined autoclave. After collecting the powder sample by centrifugation at 8000 rpm for 20 min, it was washed with MeOH by sonication and centrifuged for 20 min. This washing step was repeated two more times. The yield of the acquired CdIF-1 powder was \sim 30%.

Amorphization of CdIF-1

The as-prepared CdIF-1 particles were transferred to a 5 ml Pyrex beaker covered with aluminum foil with small holes. The beaker was then placed in the middle of a tube furnace (Thermo Scientific, USA). The sealed furnace chamber containing the sample was purged using inert argon gas at a flow rate of 200 cm³ min⁻¹ for >1 h. The amorphization experiments were conducted by heating the samples at a heating rate of 5 °C min^{-1} to various temperatures (i.e., 220-420 °C) for varying times (0-480 min). After the heat-treatment, the furnace was cooled down naturally prior to collecting the samples.

Characterization

Thermogravimetric analysis (TGA) was performed using a Q50 (TA instruments) in the temperature range of 25–800 °C at a 5 °C min⁻¹ ramp rate under an air flow of 50 cm³ min⁻¹. Differential scanning calorimetry (DSC) was conducted using a Q20 (TA instruments) in the temperature range of 25 °C to 420 °C at a ramping rate of 5 °C min⁻¹ under an argon flow of 100 cm³ min⁻¹. X-ray diffraction (XRD) patterns were obtained using an X-ray diffractometer (Rigaku Miniflex II) in the 2θ range of 5–30° with Cu-K α radiation ($\lambda = 1.5406$ Å). Scanning electron micrographs were collected using an electron microscope (SEM, JEOL JSM-7500F) at an acceleration voltage of 5 keV with a 15 mm working distance. Transmission electron microscopy (TEM) analysis was conducted using a FEI Tecnai G2 F20 Super-Twin FE-TEM operating at 120 keV. TEM samples were prepared by microtoming. Vibrational spectra were collected using a Fourier transform-infrared spectrometer (FT-IR, Nicolet iS5 Thermo Scientific) equipped with an attenuated total reflectance (ATR, iD7) accessory at a wavenumber of 4000-400 cm⁻¹ with a resolution of 4 cm⁻¹ and 16 scans.

Gas adsorption measurements

Prior to gas adsorption measurements, the samples were degassed at 150 °C under vacuum for >8 h. N₂ physisorption was performed using an ASAP 2020 plus (Micromeritics) at a relative pressure from 10^{-5} to 0.99 at 77 K. The same instrument was used to obtain adsorption isotherms of H2, N2, CO2, CH4, C2H4, C_2H_6 , C_3H_6 , C_3H_8 , n- C_4H_{10} , and i- C_4H_{10} at an absolute pressure spanning from 0.5 to 760 mmHg at two different temperatures, 0 °C and 25 °C. The isosteric heat of sorption (ΔH_{ads}°) for C_2H_4 , C_2H_6 , C_3H_6 , C_3H_8 , n- C_4H_{10} , and i- C_4H_{10} was estimated using eqn (1) by fitting the virial type equation (eqn (2)). 42,43

$$\Delta H_{\rm ads}^{\circ} = R \times a_0 \tag{1}$$

$$\ln(p) = \ln(n) + \frac{1}{T} \sum_{i=0}^{m} a_i n^i + \sum_{i=0}^{n} b_i n^i$$
 (2)

where p is pressure (mmHg), n is the amount of adsorbed gases (mmol g^{-1}), T is temperature (K), R is the ideal gas constant, a_i and b_i are virial coefficients, and m and n represent the numbers of coefficients, which were determined until the fitting results met the R^2 value of >0.99. Kinetic uptake results were obtained at p = 0.5 mmHg using a rate of adsorption (ROA) software provided by Micromeritics. Given the relatively high surface resistance compared to the internal diffusion resulting from the small particle size, the Fickian transport diffusivity (D) was estimated using eqn (3)44-46 at a fractional uptake of 0.2-0.6.47,48

$$\frac{n_t}{n_\infty} \approx \frac{6}{\sqrt{\pi}} \sqrt{\frac{Dt}{r^2}} \tag{3}$$

where n_t and n_{∞} are the amounts of adsorbed gases at time t and at equilibrium, respectively, and r (cm) is the radius of particles. The kinetic measurements were carried out in a triplicate manner. For gas molecules exhibiting Langmuir-type isotherms, the corrected diffusivity (D_0) (i.e., intrinsic mobility) can be estimated by applying eqn (4).49

$$D = \frac{D_0}{1 - \theta} \tag{4}$$

The fractional surface coverage (i.e., $\theta = n(p)/n_s$) was obtained from the Langmuir equation (eqn (5)).

$$\theta = \frac{n(p)}{n_{\rm s}} = \frac{b \times p}{1 + b \times p} \tag{5}$$

where p is the equilibrium pressure (mmHg), n(p) is the amount adsorbed (mmol g^{-1}), n_s is the capacity constant (mmol g^{-1}), and b is the affinity constant (mmHg $^{-1}$). The activation energy of diffusion (E_a) was calculated using an Arrhenius-type equation using D_0 values measured at three different temperatures (i.e., 0 °C, 25 °C and 50 °C).

Conclusions

In conclusion, we reported the first example of thermallyinduced amorphization of a SOD ZIF, CdIF-1, and successfully demonstrated the tuning of its aperture size by controlled

thermal amorphization. The long-range order of CdIF-1 started to disappear at 220 °C likely from the relatively high-energy defective sites, whereas the short-range order were preserved. The amorphization increased the framework density, resulting in a substantially reduced N2 uptake at 77 K. At ambient temperature, however, the partially amorphized CdIF-1 samples (a_TCdIF-1) showed accessible pores even for large gas molecules such as C₄ isomers possibly due to the enhanced framework flexibility resulting from amorphization and thermal energy. The amorphous CdIF-1 revealed the clear molecular cut-offs based on the sizes of gas molecules, and the cut-offs were shifted to a smaller size as the extent of amorphization increased. The n-C₄H₁₀/i-C₄H₁₀ diffusivity selectivity of CdIF-1 was changed from 1.5 to 8.5, to 40.7, and to 15.3 as the extent of amorphization increased to 30%, to 70%, and to 100%, respectively. Furthermore, the n-C₄H₁₀/i-C₄H₁₀ adsorption selectivity was increased more than four-fold from 1.1 up to 4.9 at \sim 1 atm. The dramatically improved molecular sieving effects of CdIF-1 upon controlled thermal amorphization can be attributed to the tuning of the effective aperture of CdIF-1.

Conflicts of interest

There are no conflicts to declare.

Acknowledgements

H.-K. J. acknowledges the financial support from the National Science Foundation (CBET-1929596). This publication was made possible in part by NPRP grant # 12S-0209-190064 from the Qatar National Research Fund (a member of Qatar Foundation). The findings achieved herein are solely the responsibility of the authors. The National Science Foundation supported the FE-SEM acquisition under Grant DBI-0116835, the VP for Research Office, and the Texas A&M Engineering Experimental Station.

References

- 1 K. S. Park, Z. Ni, A. P. Cote, J. Y. Choi, R. D. Huang, F. J. Uribe-Romo, H. K. Chae, M. O'Keeffe and O. M. Yaghi, Proc. Natl. Acad. Sci. U. S. A., 2006, 103, 10186-10191.
- 2 H. Furukawa, K. E. Cordova, M. O'Keeffe and O. M. Yaghi, Science, 2013, 341, 974-986.
- 3 J. J. Yang, Y. B. Zhang, Q. Liu, C. A. Trickett, E. Gutierrez-Puebla, M. A. Monge, H. J. Cong, A. Aldossary, H. X. Deng and O. M. Yaghi, J. Am. Chem. Soc., 2017, 139, 6448-6455.
- 4 H. K. Jeong, AIChE J., 2021, 67, e17258.
- 5 K. H. Li, D. H. Olson, J. Seidel, T. J. Emge, H. W. Gong, H. P. Zeng and J. Li, J. Am. Chem. Soc., 2009, 131, 10368-
- 6 H. T. Kwon and H. K. Jeong, J. Am. Chem. Soc., 2013, 135,
- 7 K. C. Jayachandrababu, D. S. Sholl and S. Nair, J. Am. Chem. Soc., 2017, 139, 5906-5915.

- 8 J. A. Thompson, C. R. Blad, N. A. Brunelli, M. E. Lydon, R. P. Lively, C. W. Jones and S. Nair, Chem. Mater., 2012, 24, 1930-1936.
- 9 F. Hillman, J. Brito and H. K. Jeong, ACS Appl. Mater. Interfaces, 2018, 10, 5586-5593.
- 10 K. Eum, M. Hayashi, M. D. De Mello, F. Xue, H. T. Kwon and M. Tsapatsis, Angew. Chem., Int. Ed., 2019, 58, 16390-16394.
- 11 F. Hillman, J. M. Zimmerman, S. M. Paek, M. R. A. Hamid, W. T. Lim and H. K. Jeong, J. Mater. Chem. A, 2017, 5, 6090-6099.
- 12 P. Krokidas, S. Moncho, E. N. Brothers, M. Castier and I. G. Economou, Phys. Chem. Chem. Phys., 2018, 20, 4879-4892.
- 13 S. Zhou, Y. Y. Wei, L. B. Li, Y. F. Duan, Q. Q. Hou, L. L. Zhang, L. X. Ding, J. Xue, H. H. Wang and J. Caro, Sci. Adv., 2018, 4, 1393-1400.
- 14 Q. Q. Hou, Y. Wu, S. Zhou, Y. Y. Wei, J. Caro and H. H. Wang, Angew. Chem., Int. Ed., 2019, 58, 327-331.
- 15 D. J. Babu, G. W. He, J. Hao, M. T. Vandat, P. A. Schouwink, M. Mensi and K. V. Agrawal, Adv. Mater., 2019, 31, 1900855-1900860.
- 16 Y. J. Ban, Z. J. Li, Y. S. Li, Y. Peng, H. Jin, W. M. Jiao, A. Guo, P. Wang, Q. Y. Yang, C. L. Zhong and W. S. Yang, Angew. Chem., Int. Ed., 2015, 54, 15483-15487.
- 17 S. Li, R. Limbach, L. Longley, A. A. Shirzadi, J. C. Walmsley, D. N. Johnstone, P. A. Midgley, L. Wondraczek and T. D. Bennett, J. Am. Chem. Soc., 2019, 141, 1027-1034.
- 18 S. Conrad, P. Kumar, F. Xue, L. M. Ren, S. Henning, C. H. Xiao, K. A. Mkhoyan and M. Tsapatsis, Angew. Chem., Int. Ed., 2018, 57, 13592-13597.
- 19 Y. H. Wang, H. Fin, Q. Ma, K. Mo, H. Z. Mao, A. Feldhoff, X. Z. Cao, Y. S. Li, F. S. Pan and Z. Y. Jiang, Angew. Chem., Int. Ed., 2020, 59, 4365-4369.
- 20 T. D. Bennett, A. L. Goodwin, M. T. Dove, D. A. Keen, M. G. Tucker, E. R. Barney, A. K. Soper, E. G. Bithell, J. C. Tan and A. K. Cheetham, Phys. Rev. Lett., 2010, 104, 115503-115506.
- 21 T. D. Bennett and A. K. Cheetham, Acc. Chem. Res., 2014, 47, 1555-1562.
- 22 T. D. Bennett, D. A. Keen, J. C. Tan, E. R. Barney, A. L. Goodwin and A. K. Cheetham, Angew. Chem., Int. Ed., 2011, 50, 3067-3071.
- 23 T. D. Bennett, S. Cao, J. C. Tan, D. A. Keen, E. G. Bithell, P. J. Beldon, T. Friscic and A. K. Cheetham, J. Am. Chem. Soc., 2011, 133, 14546-14549.
- 24 K. W. Chapman, G. J. Halder and P. J. Chupas, J. Am. Chem. Soc., 2009, 131, 17546-17547.
- 25 S. H. Lapidus, G. J. Halder, P. J. Chupas and K. W. Chapman, J. Am. Chem. Soc., 2013, 135, 7621-7628.
- 26 C. Zhou, L. Longley, A. Krajnc, G. J. Smales, A. Qiao, I. Erucar, C. M. Doherty, A. W. Thornton, A. J. Hill, C. W. Ashling, O. T. Qazvini, S. J. Lee, P. A. Chater, N. J. Terrill, A. J. Smith, Y. Z. Yue, G. Mali, D. A. Keen, S. G. Telfer and T. D. Bennett, Nat. Commun., 2018, 9,
- 27 L. Frentzel-Beyme, M. Kloss, P. Kolodzeiski, R. Pallach and S. Henke, J. Am. Chem. Soc., 2019, 141, 12362-12371.

- 28 L. Frentzel-Beyme, M. Kloss, R. Pallach, S. Salamon, H. Moldenhauer, J. Landers, H. Wende, J. Debus and S. Henke, J. Mater. Chem. A, 2019, 7, 985–990.
- 29 X. L. Ma, P. Kumar, N. Mittal, A. Khlyustova, P. Daoutidis, K. A. Mkhoyan and M. Tsapatsis, *Science*, 2018, **361**, 1008–1011.
- 30 D. A. Keen and T. D. Bennett, *Phys. Chem. Chem. Phys.*, 2018, **20**, 7857–7861.
- 31 Y. Q. Tian, S. Y. Yao, D. Gu, K. H. Cui, D. W. Guo, G. Zhang, Z. X. Chen and D. Y. Zhao, *Chem.-Eur. J.*, 2010, **16**, 1137– 1141.
- 32 E. F. Baxter, T. D. Bennett, A. B. Cairns, N. J. Brownbill, A. L. Goodwin, D. A. Keen, P. A. Chater, F. Blance and A. K. Cheetham, *Dalton Trans.*, 2016, 45, 4258–4268.
- 33 R. Gaillac, P. Pullumbi and F. X. Coudert, *J. Phys. Chem. C*, 2018, **122**, 6730–6736.
- 34 C. H. Wu, D. G. Xie, Y. J. Mei, Z. F. Xiu, K. M. Poduska, D. C. Li, B. Xu and D. F. Sun, *Phys. Chem. Chem. Phys.*, 2019, 21, 17571–17577.
- 35 R. Gaillac, P. Pullumbi, K. A. Beyer, K. W. Chapman, D. A. Keen, T. D. Bennett and F. X. Coudert, *Nat. Mater.*, 2017, **16**, 1149–1154.
- 36 A. Kertik, L. H. Wee, M. Pfannmoller, S. Bals, J. A. Martens and I. F. J. Vankelecom, *Energy Environ. Sci.*, 2017, **10**, 2342–2351.
- 37 R. N. Widmer, G. I. Lampronti, N. Casati, S. Farsang, T. D. Bennett and S. A. T. Redfern, *Phys. Chem. Chem. Phys.*, 2019, **21**, 12389–12395.

- 38 M. Agrawal and D. S. Sholl, ACS Appl. Mater. Interfaces, 2019, 11, 31060–31068.
- 39 Y. F. He and N. A. Seaton, Langmuir, 2005, 21, 8297-8301.
- 40 S. H. Madani, C. Hu, A. Silvestre-Albero, M. J. Biggs, F. Rodriguez-Reinoso and P. Pendleton, *Carbon*, 2016, 96, 1106–1113.
- 41 J. Z. Sun, L. Semenchenko, W. T. Lim, M. F. Rivas, V. Varela-Guerrero and H. K. Jeong, *Microporous Mesoporous Mater.*, 2018, **264**, 35–42.
- 42 A. Nuhnen and C. Janiak, *Dalton Trans.*, 2020, **49**, 10295–10307.
- 43 H. J. Park and M. P. Suh, Chem. Sci., 2013, 4, 685-690.
- 44 A. Davarpanah and B. Mirshekari, *Ind. Eng. Chem. Res.*, 2019, 58, 12392–12400.
- 45 C. Zhang, R. P. Lively, K. Zhang, J. R. Johnson, O. Karvan and W. J. Koros, *J. Phys. Chem. Lett.*, 2012, 3, 2130–2134.
- 46 S. Park and H. K. Jeong, J. Mater. Chem. A, 2020, 8, 23645-23653.
- 47 N. G. Rincon-Silva, J. C. Moreno-Pirajan and L. Giraldo, *Adsorption*, 2016, 22, 33–48.
- 48 S. Tanaka, K. Fujita, Y. Miyake, M. Miyamoto, Y. Hasegawa, T. Makino, S. Van der Perre, J. C. Saint Remi, T. Van Assche, G. V. Baron and J. F. M. Denayer, *J. Phys. Chem. C*, 2015, **119**, 28430–28439.
- 49 M. S. Ray, Diffusion in Zeolites and Other Microporous Solids, John Wiley & Sons, Inc., New York, 1992.